PAPER

Check for updates

On-chip droplet analysis and cell spheroid screening by capillary wrapping enabled shape-adaptive ferrofluid transporters†

Xuejiao Wang, [iD][a] Xin Li, [iD][a] Aoyang Pu,[a] Ho Bak Shun,[a] Cien Chen,[a] Liqing Ai,[a] Zhaoling Tan,[a] Jilin Zhang,[a] Kai Liu,[a] Jun Gao, [iD] *[b] Kiwon Ban*[a] and Xi Yao [iD] *[ac]

Non-invasive droplet manipulation with no physical damage to the sample is important for the practical value of manipulation tools in multidisciplinary applications from biochemical analysis and diagnostics to cell engineering. It is a challenge to achieve this for most existing photothermal, electric stimuli, and magnetic field-based technologies. Herein, we present a droplet handling toolbox, the ferrofluid transporter, for non-invasive droplet manipulation in an oil environment. It involves the transport of droplets with high robustness and efficiency owing to low interfacial friction. This capability caters to various scenarios including droplets with varying components and solid cargo. Moreover, we fabricated a droplet array by transporter positioning and achieved droplet gating and sorting for complex manipulation in the droplet array. Benefiting from the ease of scale-up and high biocompatibility, the transporter-based droplet array can serve as a digital microfluidic platform for on-chip droplet-based bioanalysis, cell spheroid culture, and downstream drug screening tests.

Introduction

The control of micro-sized droplets with high efficiency, programmability and precision has important applications from water collection to disease diagnostics and cell engineering.[1–3] Specific applications, especially in biomedical fields, have particular requirements, such as lossless manipulation in a sealed environment (usually under oil) for reactions on a long timescale,[4] moderate operations for sensitive samples such as cells,[5] and 'all-in-one' chips for cell engineering,[6] *i.e.*, cell spheroid culture and subsequent high throughput drug screening, with a series of prerequisites which challenge most droplet manipulation strategies. Conventional droplet manipulation methods utilizing geometrically well-defined channels are confronted by the lack of programmability and reconfigurability.[7,8] To date, numerous advances have been reported to manipulate droplets by engineering nature-inspired surfaces.[9–11] However,

self-propelled droplet movement that relies on surface wetting gradients *via* topographic or chemical gradients has strong limitations, such as direction of movement, distance and speed.[12] Printing charged surfaces enriches the capability for long-distance transport with the help of additional electrostatic forces.[13] To realize high-dimensional control, a toolbox that includes the utilization of various external stimuli, such as electric,[14,15] magnetic,[16] acoustic,[17] and photothermal[18,19] stimuli, has been established.[20] Electrowetting on dielectric (EWOD) technique has revolutionized many application domains in a programmable and digital fashion.[21] However, EWOD suffers from restricted actuation volume and substrate/electrode fouling. Furthermore, other tactics that rely on photothermal and acoustic stimuli may lead to irreversible physical damage to droplets, for instance, accelerated droplet evaporation under heat input.[22]

Instead, magnetic manipulation, featuring contactless, biosafety and rapid response characteristics, has received increasing attention owing to its flexible maneuverability and high actuation precision.[23–25] In particular, magnetic control units can be minimized and integrated easily through patterning electromagnetic modules and can further be scaled up and programmed, which is promising in parallel analysis and screening.[26–28] Magnetic field (MF) as a means to handle droplets has been widely explored by adding magnetic particles into droplets.[25,29,30] Nevertheless, particle additives trigger undesired sample contamination and

[a] Department of Biomedical Sciences, Department of Infectious Diseases and Public Health, City University of Hong Kong, Tat Chee Avenue, Kowloon Tong, Hong Kong, P. R. China. E-mail: Ban.KW@cityu.edu.hk, xi.yao@cityu.edu.hk
[b] Qingdao Institute of Bioenergy and Bioprocess Technology, Chinese Academy of Sciences, Qingdao 266101, Shandong Province, P. R. China. E-mail: jun.gao@qibebt.ac.cn
[c] Shenzhen Research Institute, City University of Hong Kong, Shenzhen 518075, P. R. China
† Electronic supplementary information (ESI) available. See DOI: https://doi.org/10.1039/d3lc00906h

restrained droplet sizes. An alternative is adopting active surfaces made of, for example, magnetic-responsive substrates.[23,31] A lack of capability arises when the goal is to integrate the manipulation method into a programmed digital control system.[20] Compared with solid substrates, the flexibility of droplet manipulation can be significantly extended when it is performed on ferrofluid infused substrates.[32,33] However, droplets moving on ferrofluid-infused surfaces still experience high interfacial drag,[34] and the exposure of droplets to an open environment is not feasible for bioanalytical applications where long-term cell incubation and *in situ* observations are needed.[35]

Herein, we propose a ferrofluid transporter, which exhibits on-site droplet wrapping and transportation of droplets with high robustness in a silicone oil environment (Fig. 1A). Contrary to the most reported methods, in which responsive chemicals or particles are added inside droplets, the ferrofluid can spontaneously wrap the contact droplet through spreading on the interface of the droplet and silicone oil surroundings, indicating a non-invasive strategy. The wrapping leads to an adaptive three-phase system, and majority of the ferrofluid is settled at the bottom because of its high density. Upon the application of an external magnetic field, the ferrofluid responds to deform and acts as a transporter to carry the droplet toward the center of the magnetic field, allowing a non-contact stimulation driven mode. Owing to the non-invasive and non-contact stimulation, transporter-manipulated droplets can bear a wide range of bio-samples.

Experimental results indicate that transporter manipulation can be used for programmed digital actuation, fabricating droplet arrays, delivering droplets in an array, and holding great potential for the development of next-generation digital manipulation platforms.

Experimental methods

Materials

Monocarboxylic acid functionalized perfluoropolyether (PFPE–COOH, 157FSL) was obtained from DuPont and perfluoropolyether (PFPE, GPL 100) was purchased from Krytox. $FeCl_3$, $FeSO_4$, aqueous ammonia solution (28–30%), PEG 20000, carmine, sodium fluorescein, and dimethyl silicone were purchased from J&K. Dulbecco's modified Eagle medium (DMEM) was obtained from ThermoFisher Scientific. PBS (10×) buffer, bovine serum albumin (BSA), LB broth, and LB agar were purchased from Solarbio. Hydrochloric acid, sodium hydroxide, sodium fluorescein (46960), *N*-acetyl-L-cysteine (#A7250), L-ascorbic acid (#A4544), and 2′,7′-dichlorofluorescin diacetate (#D6883) were obtained from Sigma Aldrich. Hydrogen peroxide (#23619.297) was purchased from VWR International. All chemicals were used without further purification. Polystyrene (PS), polyethylene (PE), polyvinyl chloride (PVC), and polyethylene terephthalate (PET) containers were purchased from BKMAM and used directly without further modification. Human follicle dermal papilla cells were purchased from Promocell® (C-12071) and maintained in papilla cell media (cell applications, 611-500).
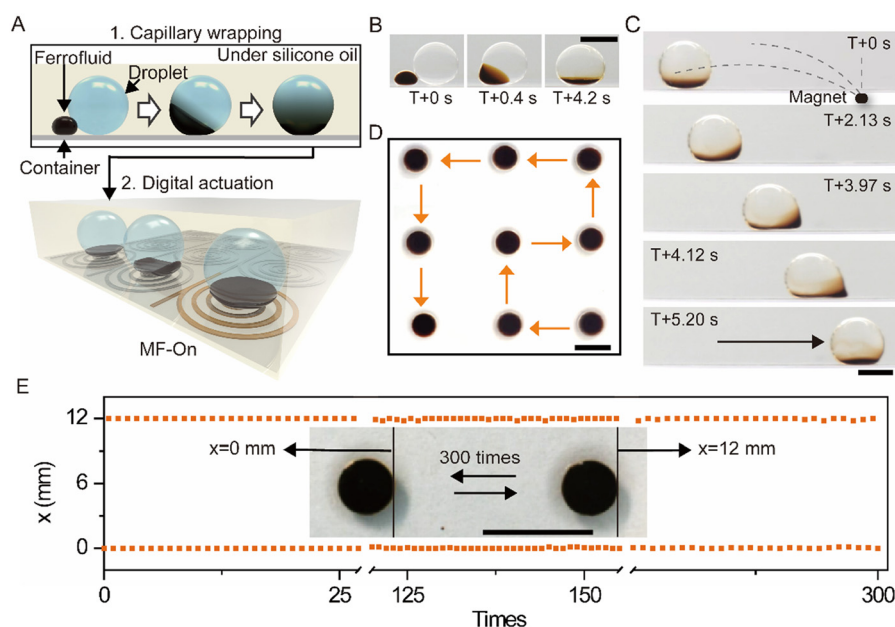

Fig. 1 Capillary wrapping enabled ferrofluid transporter for digital droplet actuation. (A) Schematic illustration of the ferrofluid exhibiting on-site wrapping and digital actuation of a droplet with magnetic field (MF) guidance under oil. (1) and (2) schematize the capillary wrapping and digital actuation process respectively. (B) Optical images show the ferrofluid (1 μL) contacting a 10 μL water droplet (left) and wrapping the water droplet (middle) until it is fully wrapped (right). (C) Actuation of the droplet by the transporter under an external magnetic field gradient. The dotted lines represent magnetic field lines. (D) Digital actuation of 10 μL droplet by 5 μL transporter follows a preplanned pathway. (E) Stability of digital transportation of the droplet by the ferrofluid transporter. The optical image in the inset shows that a droplet was transported back-and-forth. Scale bars are 2 mm in B and C and 5 mm in D and E.

Ferrofluid preparation

The ferrofluid was fabricated in our lab following a reported method.[36] First, $FeCl_3$ and $FeSO_4$ (with a Fe^{3+}/Fe^{2+} molar ratio of $3:2$) were mixed in 72 mL of DI water at room temperature under magnetic stirring with a speed of 500 rpm min^{-1} for 5 min. Then, PFPE–COOH as a stabilizer was added dropwise at a mass ratio of $1:3$ wt%. After thorough mixing, an aqueous ammonia solution (28–30%) was used to adjust the pH of the solution to initiate the coprecipitation reaction. The reaction was carried out for an hour at 95 °C. Then, the product was washed with water, ethanol, and water again, until the pH changed to 7. The residual water in the product was removed by vacuum drying at 80 °C. Finally, Krytox 100 was added to dispense modified nanoparticles with the assistance of ultrasound to obtain the ferrofluid (20 m/v%).

Instruments and characterization

Polystyrene containers were used for all experiments except the general study in Fig. 3C. The droplets and ferrofluid transporters were added to containers containing silicone oil

through a pipette or micro-syringe (the volumes were 50 μL, 1 μL, and 0.5 μL, purchased from Shanghai Gaoge Industry and Trade Co., Ltd.). The magnetic properties of fabricated Fe_3O_4 nanoparticles (68 emu g^{-1}) were measured with a vibrating sample magnetometer (Lakeshore, 8600 Series VSM). The magnetic field strength of different magnets was measured by a Gauss meter (~mT, GLTL WT103). For droplets with different pH values, the pH was adjusted by hydrochloric acid and sodium hydroxide and confirmed by a digital pH meter tester (PmoYoKo, Tabletop). Droplet movement was recorded by a commercial CCD (HIKVISION MV-CA050-20UC) with a maximum of 20 fps and a resolution of 2448 × 2048. Fluorescence images for cell culturing and screening were captured by a Nikon Eclipse Ni-E Fluorescent Microscope and droplet array imaging images were recorded by a Nikon SMZ800N.

Droplet actuation

Commercially available NdFeB was used for magnetic field generation. For the average velocity calculation, the
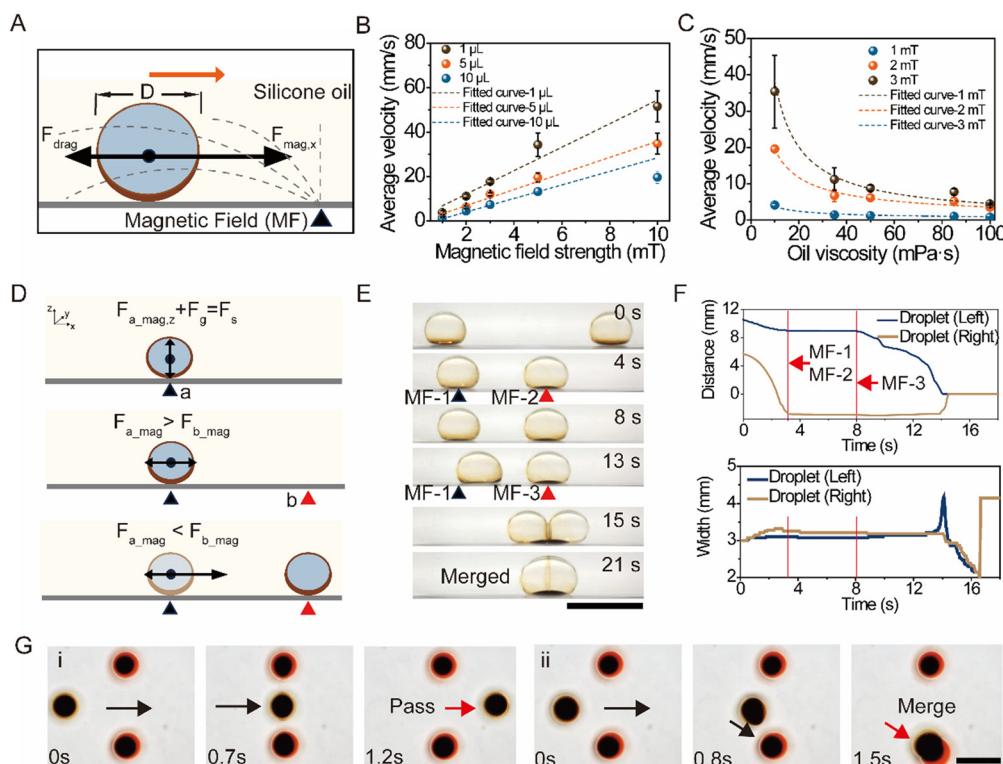

Fig. 2 Mechanistic study of the digital actuation. (A) Schematic illustration of the force analysis for transporter actuation. Two forces, magnetic force ($F_{mag.x}$) and movement resistance (F_{drag}), determined the movement. The orange arrow and gray dotted lines represent the direction of actuation and magnetic lines, respectively. (B) Effect of the magnetic field on average velocity. The volume of the transporter was 1 μL. All values represent mean ± SD for $n = 3$ independent experiments. (C) Effect of the dynamic viscosity of silicone oil on average velocity. The droplet and transporter had a volume of 1 μL. All values represent mean ± SD for $n = 3$ independent experiments. (D) Schematic diagram of controllable droplet behavior by tuning the magnetic field strength. Positions a and b are two locations where a magnetic field was applied. F_s represents the sum of the buoyancy force on the droplet and the normal force from the bottom surface. (E) Sequential snapshots for controlled droplet positioning and transportation. The magnitude of magnetic forces is as follows: $F_{MF-1} = F_{MF-2} < F_{MF-3}$. MF-2 and MF-3 were at the same location. (F) Measured distance and width of two droplets against time in (E). The width refers to the length of droplets observed from a side-view. (G) Droplet gating and sorting. A droplet (10 μL) was transported to pass through two droplets (each was 10 μL) (i) and specifically merged with one droplet (ii). The volume of transporters was 1 μL. Positioned droplets were dyed with carmine (0.05 wt% in water). Scale bars are 5 mm.
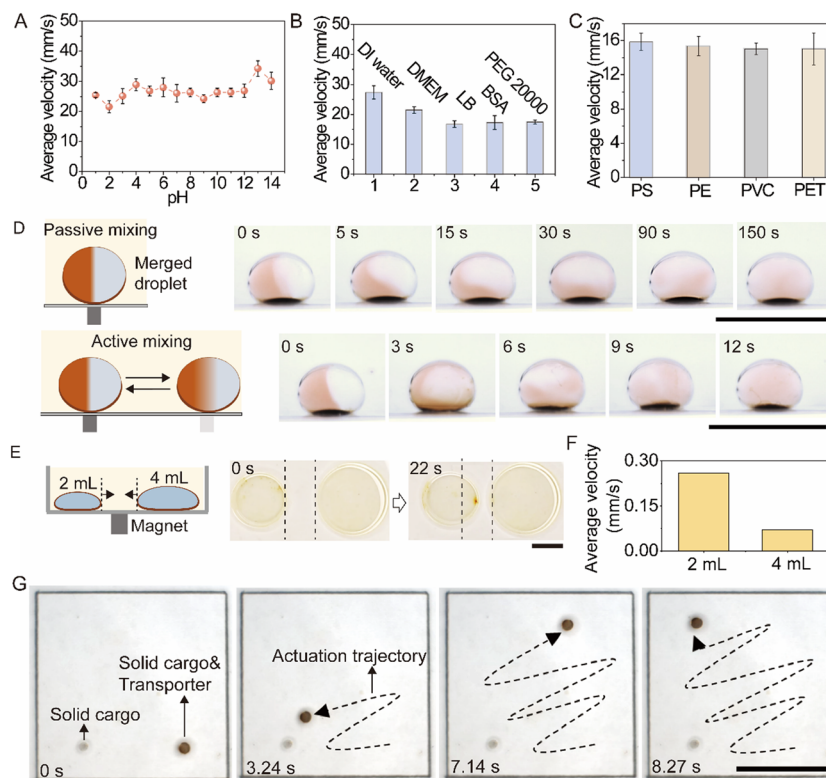
Fig. 3 Generality of the ferrofluid transporter. (A) Average velocity of droplets (1 μL) with different pH ranges from 1 to 14. The volume of the transporter was 1 μL. All values represent mean ± SD for $n = 3$ independent experiments. (B) Average velocities of droplets with a volume of 1 μL containing different biochemical reagents displayed no significant difference. The volume of the transporter was 1 μL. All values represent mean ± SD for $n = 3$ independent experiments. (C) Compatibility of the actuation method on different substrates. The volumes of droplets and the transporter were all 1 μL. All values represent mean ± SD for $n = 3$ independent experiments. (D) Time-lapsed images show the mixing of droplets under passive mixing without transportation and active mixing through back-and-forth transportation. Two droplets (each has a volume of 5 μL) with one dyed with carmine were first transported to merge with each other, and the time they merged was set at 0 s. For active mixing, the droplet was moved back and forth once in 3 seconds. (E) Actuation capability for droplets with a large volume difference from the transporter. The magnetic flux density for large-volume droplet actuation was about ~35 mT. The dotted line is the transportation baseline. (F) Calculated average velocity for droplets in D at 22 s. (G) Transportation of solid cargo. Scale bars are 5 mm in D and 10 mm in E and G.

magnet was placed 10 cm away from the droplet, and the time for droplets to move to the magnetic field center was recorded. For the digital actuation in Fig. 1D, a NdFeB magnet ($d \times l = 2 \times 3$ mm, ~1 mT) placed in a 3D printed container (printed by Phrozen Sonic 4K Resin 3D Printer) together with a coil cylinder (radius 0.5 mm, thickness 1 mm, made of a coil with a diameter of 0.25 mm) on the top forms one electromagnetic unit. A DC source was connected to the pre-assembled coil cylinder (radius 0.5 mm, thickness 1 mm, made of a coil with a diameter of 0.25 mm) through a controllable power supply (MAISHENG®, DC power supply). The circuit was connected to a switch controller and connected to the wireless sensor remote controller for digital droplet actuation. A 5 ohm resistor was connected to the circuit to prevent short circuiting.

Array fabrication and droplet delivery

A patterned iron needle (commercially available, with an interval of 2.54 mm) was placed onto a NdFeB magnet ($d \times$

$h = 2 \times 3$ mm, ~35 mT) for magnetic field arraying in Fig. 4A. Miniaturized permanent magnets with a diameter of 0.5 mm and a height of 1 mm were used in Fig. 4B and for drug screening in Fig. 6. Then, the ferrofluid was added and pinned to each magnetic field center using a pipette to obtain the ferrofluid array. The ferrofluid volumes for fabricating 8×9, 5×6, and 5×5 arrays were 10 μL, 5 μL, and 1 μL, respectively. Then, the droplet array was obtained by pipetting droplets to each pinned ferrofluid. For droplet delivery in the array, a magnet with the same size of magnets in the array was manually controlled to guide the transporter.

Real-time quantitative reverse transcription PCR (qRT-PCR)

Total RNA was extracted from rhabdomyosarcoma (RD) cells with TRIzol reagent (Ambion, Life Technologies). Quantitative real-time PCR (qRT-PCR) was carried out with SYBR Green Mix (Life Technologies) on an applied Biosystems StepOne real-time PCR system. The primer sequences of GAPDH mRNA were as follows: 5′-GTCTCCTCTGACTTCAACAGCG-3′
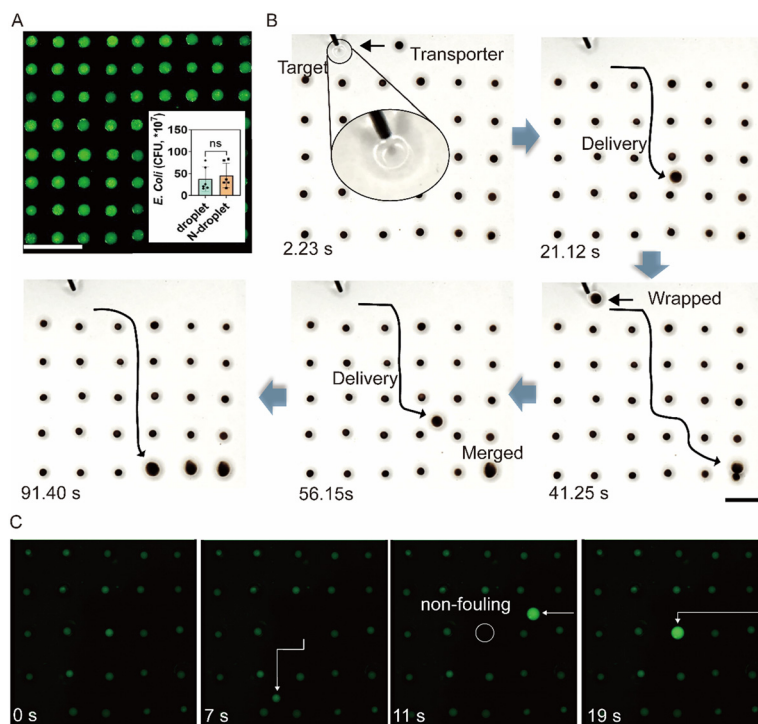
Fig. 4 Transporter manipulated on-chip droplet array and target delivery. (A) Fluorescent images of 72 droplets (1 μL for each) containing *E. coli* on the transporter-manipulated array after 24 h of incubation. The inset is the plate count number of the colony from six droplets and six non-droplet incubations. (B) Delivery of target droplets in transported-manipulated droplet array. On a chip with an array of droplets (each droplet has a volume of 1 μL), a micro-syringe was used to inject a target droplet (5 μL) onto the chip, following the transporter was guided to wrap and transport the target to merge with specific droplets in the array. (C) Time-lapse fluorescent images showing the repeatable and cyclic manipulation of the transporter-manipulated droplet chip. Sodium fluorescein was adopted for visualization. Scale bars are 5 mm in A and B and 2 mm in C.
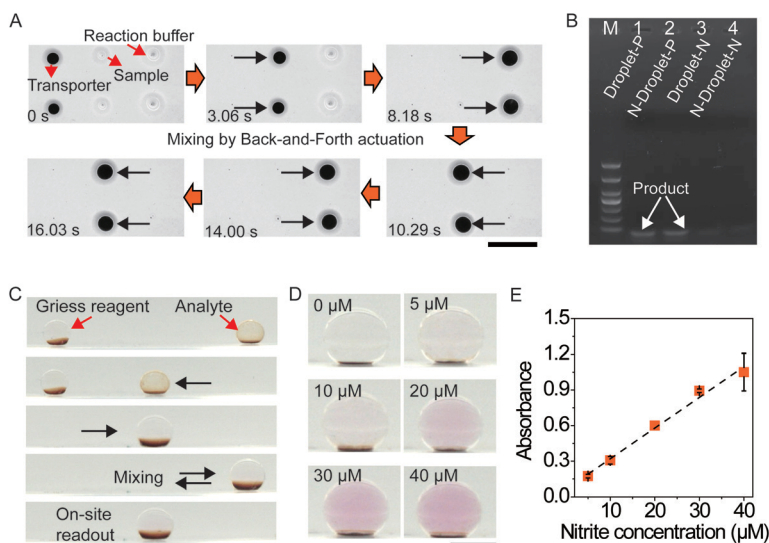

Fig. 5 On-chip droplet-based biochemical analysis. (A) The transporter performed digital actuation for polymerase chain reaction. Transporter executed sample carrying, transportation, droplet merging, and mixing sequentially. (B) Polyacrylamide gel electrophoresis (PAGE) results of PCR products with pre-process in tube and on-chip separately. (C) Digital actuation of the transporter for nitrite detection. (D) Images of final products in (C) were captured and displayed. (E) Measured absorbance shows a good linearity at measured concentrations. All values represent mean ± SD for *n* = 3 independent experiments. Scale bars are 10 mm in A and C and 2 mm in D.

(forward) and 5′-ACCACCCTGTTGCTGTAGCCAA-3′ (reverse). The target (2 μL) droplet and reaction buffer (8 μL) were

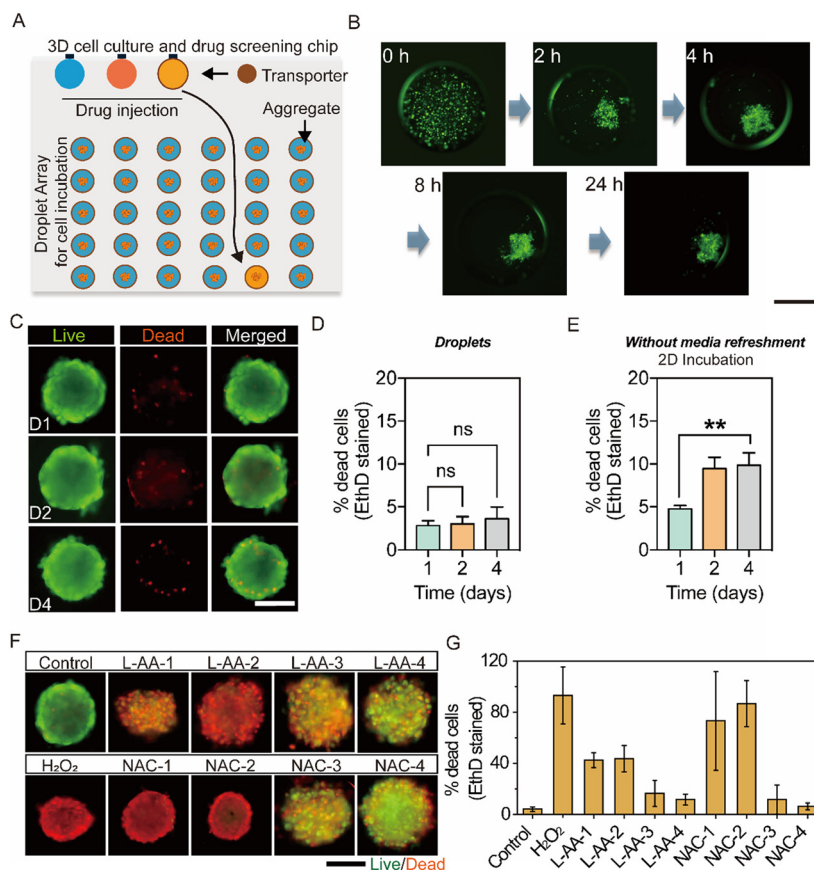mixed through back-and-forth movement. Then, the mixed droplet was directly taken out for amplification, and the

Fig. 6 'All in one' chip for cell spheroid culture and drug screening. (A) Schematic of the transporter-manipulated chip with incubation area and drug delivery capability. (B) Time-lapsed images showing the aggregation of HFDPC cells within the droplet. The majority of cells migrate and aggregate at the bottom of droplets after incubation for 2 h. (C) Fluorescence images of live/dead-stained human follicle dermal papilla cells (HFDPCs) on day 1 (D1), day 2 (D2), and day 4 (D4). (D) Quantification of the percentage of dead cells in aggregated spheres. All values represent mean ± SD for $n = 3$ independent experiments. (E) Quantification of the percentage of dead cells cultured in the monolayer without media refreshment. All values represent mean ± SD for $n = 3$ independent experiments. Merged images (F) and quantified dead cells (G) show the effect of L-ascorbic acid (L-AA) (10/100/150/200 μM for L-AA-1 to L-AA-4, respectively) and N-acetyl cysteine (NAC) (4/20/30/40 mM for NAC-1 to NAC-4, respectively) on H_2O_2-treated HFDPC. All values represent mean ± SD for $n = 3$ independent experiments. Scale bars are 500 μm in B and 100 μm in C and F.

agarose gel was utilized for the verification of the product compared to the control group (all steps were carried out in a PCR tube).

Griess test

Nitrite detection was realized by using a Griess reagent kit (Invitrogen, catalog number: G7921). First, equal volumes of N-(1-naphthyl)ethylenediamine and sulfanilic acid were mixed to obtain the Griess reagent according to the manual, and deionized water was utilized to dilute the standard nitrite solution into different concentrations. Next, 5 μL of Griess reagent (one-fold diluted) and 5 μL of detection droplet were sequentially actuated to the capture center and merged with the assistance of the magnetic field. The mixture was allowed to react for 30 min at room temperature (25 °C). The signal of different droplets was measured using a UV-vis spectrometer (NanoDrop 2000, Thermo Scientific).

Bacterial culture

Home-cultivated green fluorescent protein (GFP) dyed *E. coli* was used for the biocompatibility study. The culture medium was Luria-Bertani broth made by mixing 25 g of broth powder (Invitrogen) with 1 L of distilled water. The LB broth was sterilized at 121 °C for 20 min and stored at 4 °C before use. The concentrations of the original culturing sample and cultured samples were calculated by plate count. The initial concentration for the bacterial culture was 3×10^4 CFU. For the bacterial culture in an 8×9 droplet array, 1 μL of the droplet containing GFP-*E. coli* was added using a pipette. The droplet array was incubated at 37 °C for 24 hours.

3D cell culture

HFDPC at passages 5–8 were used for experiments. When 70–80% confluency was reached, HFDPC were detached by Accutase (Gibco, A1110501) and counted using countless automated cell counters (Invitrogen, AMQAX1000) after being

stained by trypan blue (Invitrogen, T10282). The concentration of cells is about ~1000 cells per μL, which is calculated by trypan blue using the chamber slide on an AMQAX1000: Countess™ II Automated Cell Counter. The cell solution was gently mixed before sampling to obtain droplets with uniform cell concentration.

Cell viability

Cell viability was monitored using a live/dead viability/cytotoxicity kit (Invitrogen, L3224) according to manufacturer's instructions. Briefly, Dulbecco's modified Eagle medium (DMEM) without phenol red (Gibco, 11054001) containing calcein-AM (2 μM) and ethidium homodimer-1 (4 μM) dye was mixed with droplets and incubated for 25 min at room temperature. The labelled cells were analysed with a fluorescence microscope, and the number of EthD-1-stained dead cells was calculated by ImageJ software. The percentage of dead cells in the 3D cell sphere was calculated as a ratio between the area and number of dead cells.

Intracellular reactive oxygen (ROS) detection

Intracellular reactive oxygen (ROS) levels were detected using the probe 2′,7′-dichlorodihydrofluorescein diacetate (DCFDA) (Sigma, D6883). When DCFDA is oxidized by ROS, it will convert to fluorescent 2′,7′-dichlorofluorescein (DCF). PBS containing 20 mM DCFDA was mixed with droplets and incubated at 37 °C for 30 min in the dark. The fluorescence was checked under a fluorescence microscope and measured by the acquisition of green signals, providing a radiometric indication of total ROS content. All treated samples used the same exposure time.

Results and discussion

Capillary wrapping enabled ferrofluid transporter for digital droplet actuation

Fig. 1A shows a schematic of the ferrofluid transporter wrapping and digitally transportation of a water droplet. The droplet manipulation was performed in a transparent polystyrene container filled with silicone oil. In this submerged system, water and fluorinated ferrofluid (made of Fe_3O_4 nanoparticles with a main diameter of 32 nm, Fig. S2†) droplets exhibit a spherical shape when put on the container surface (Fig. S3†). In a typical case (Movie S1 and Fig. S1†), a small droplet (1 mL) of ferrofluid was placed adjacent to a larger water droplet (10 mL), in a bath of silicone oil. Upon applying a magnetic field to the location of the water droplet, the ferrofluid was actuated and approached the water droplet. As soon as the ferrofluid contacted the water droplet, it spontaneously wrapped around the water droplet and mostly accumulated at the bottom of the water droplet because of its high density (Fig. 1B). The wrapping process is driven by the energy-favorable spreading of the fluorinated ferrofluid on the surface of the water droplet, which is

modulated by the surface energy relationship of three liquid components (Note S1, ESI†). The magnetic force exerted by the magnetic field gradient actuates the ferrofluid to move toward the strong center of the magnetic field. Therefore, the ferrofluid can act as an active transporter to move the wrapped droplet under a magnetic field gradient. Experimentally, a magnet was placed at a distance from the wrapped droplet to generate a magnetic field gradient. As depicted in Fig. 1C (Movie S2†), the droplet was successfully transported, undergoing a typical process of accelerated and deaccelerated motions (Fig. S4†) and eventually positioned at the center of the magnetic field at 5.20 s. Due to the fluid nature, the ferrofluid in response to the non-uniform magnetic field deforms nonlinearly, which can change the distribution of the ferrofluid around the droplet and stretches the droplet during movement. The closer to the magnetic field center, the more obvious the change of the distribution. Fig. 1C shows that the ferrofluid obviously deforms at 4.12 s, and the wrapped droplet deforms because of the stretching.

One of the advantages of magnetic actuation is that the magnetic field can be programmed for digital control. Because the transporter actuates droplets in response to a magnetic field gradient, a magnetic digital-control system (Fig. S5†) was adopted to verify the potential for programmed digital actuation. As the magnetic field was sequentially switched on and off, an exemplary result shows that a droplet (10 mL) was successfully transported following a preplanned route, manifesting the programmability of ferrofluid transporter for digital actuation (Fig. 1D and Movie S3†). To verify the stability of the ferrofluid transporter for digital actuation, the wrapped droplet was transported from left ($x = 0$ mm) to right ($x = 12$ mm) and back to left ($x = 0$ mm) 300 times, as depicted in Fig. 1E (the inset). The location of the droplet was measured every time after it was transported, and Fig. 1E shows that the droplet was successfully transported at the 300th time, implying the good actuation stability of ferrofluid transporter.

Mechanistic study for the digital droplet manipulation

To further understand the transporter actuation, we conducted mechanism analysis of the system. In general, the wrapped droplet can be considered as a whole. Two forces primarily determine the droplet movement. The magnetic force: $F_{mag,x} = M dB_x/dx$, which is exerted by an external magnetic field, dominates the actuation, where B_x is the magnetic flux density in the x direction and M is the magnetization of the integration. The other force is the drag force (static friction), which is given by: $F_{drag} = F_f + F_h$ (Fig. 2A, ESI† text), where F_h is derived from the contact angle hysteresis, and F_f is the interfacial friction. When $F_{mag,x}$ overcomes F_{drag}, the droplet will be transported. During movement, the droplet will mainly experience viscous resistance from silicone oil considering that F_h and F_f are negligible (Fig. S6†). Thus, the resistance during

transportation can be simplified as: $F_{drag} = F_v$, and the viscous drag force can be given by: $F_v = 3\pi D\eta v$, where η is the dynamic viscosity of the silicone oil, v is the moving velocity of the ferrofluid-wrapped droplet, and D is the diameter of the wrapped droplet. The force balance can be described by an equation involving the barycenter position x:

$$\boldsymbol{M}\frac{\mathrm{d}B_x}{\mathrm{d}x} - 3\pi D\eta\frac{\mathrm{d}x}{\mathrm{d}t} - m_{w+d}\frac{\mathrm{d}^2x}{\mathrm{d}t^2} = 0, \quad (1)$$

where $\boldsymbol{M}$ is the magnetization of the ferrofluid, determined by $\boldsymbol{M} = V_w\chi\dfrac{B_0}{\mu}$. χ is the susceptibility of the ferrofluid, B_0 is the magnetic flux density of the magnet, μ is the magnetic permeability of the ferrofluid ($\sim4\pi \times 10^{-7}$ N A^{-2}), and m_{d+w} is the mass of the transporter (w) and droplet (d). Assuming a constant magnetic field gradient, we can calculate the average velocity of droplet transportation from formula (1) as:

$$\bar{v} = \beta/\alpha + \beta(e^{-\alpha t} - 1)/\alpha^2 t \quad (2)$$

with $\alpha = (3\pi D\eta)/m_{d+w}$ and $\beta = \boldsymbol{M}/m_{d+w}\dfrac{\mathrm{d}B_x}{\mathrm{d}x}$. Detailed discussion can be found in Note S2 (ESI†). Although various parameters cannot be given accurately, the influence of important factors on the transportation can be clarified from formula (2). Assuming that the droplets are of the same size and the viscosity is constant, α can be considered a constant. Theoretically, the average velocity $\bar{v}$ is approximately proportional to $\boldsymbol{M}$. We tested the average velocity of droplets of same size under different magnetic fields (Fig. 2B), and the average velocity increases with increasing magnetic flux density. When the applied magnetic field was 10 mT, the average velocity for a 1 μL droplet reached 51 mm s^{-1}. The fitted curves of tested results for different droplets indicate that the average velocity is a linear function of the magnetic flux density. Besides, if the droplet size and magnetic flux density are fixed, the time-dependent part can be dismissed because of the large order of magnitude of α ($\sim10^3$). Therefore, the average velocity of the droplet is inversely proportional to the silicone oil viscosity, theoretically. We tested the average transportation velocity for droplets with a volume of 1 μL under the same magnetic flux density (1 mT, 2 mT, and 3 mT) in silicone oils with different dynamic viscosities (Fig. 2C), and the average velocity decreased with increasing viscosity of the silicone oil. The fitted curve shows an inverse functional relationship with silicone oil viscosity, which is consistent with the trend from theoretical analysis. Regardless of the viscosity of the silicone oil, increasing the magnetic field strength can also increase the average velocity. As depicted in Fig. 2C, the average velocity was 8.74 mm s^{-1} when the magnetic flux density was 3 mT, which is higher than 1.13 mm s^{-1} when the magnetic flux density was 1 mT. Overall, the average velocity of droplets can be adjusted by managing the magnetic flux density. Detailed analysis can be found in Note S3 (ESI†).

By adjusting the net force through programming the magnetic field, it is possible to control the positioning and movement of droplets for on-demand spatiotemporal manipulation. As shown in Fig. 2D, a droplet is positioned on the magnetic field center as it is subject to the strongest magnetic force in the direction of the z-axis (Fig. 2D, top). When applying another magnetic field at position b, satisfying $F_{a\_mag} > F_{b\_mag}$ (Fig. 2D, middle), the droplet will remain positioned because of the weak interaction between the droplet and new magnetic field. Instead, if the magnetic force acting on the droplet satisfies $F_{a\_mag} < F_{b\_mag}$) (Fig. 2D, bottom), the droplet is transported to the new magnetic field center at b. To verify the controllability, two droplets were first actuated to the adjacent magnetic field center (with equal magnetic flux density) at positions MF-1 and MF-2 (Fig. 2E and Movie S4†). The two droplets remained positioned. This is because, for each droplet, the magnetic force acting on the transporter from another place is weak. Upon replacing with a stronger magnetic field (from MF-2 to MF-3), the droplet on the left started to move and finally merged with the droplet on the right, because the magnetic force of MF-3 acting on the transporter on the left exceeded the force from MF-1. In Fig. 2F, the width information shows the deformation of the two droplets responding to the magnetic fields as well as the merging process of the two droplets. When applying MF-1 and MF-2 in the system, each droplet deforms slightly during movement (Fig. 2F, bottom). However, upon applying the strong magnetic field MF-3, especially when approaching the center where the magnetic flux density is enhanced, the droplet is greatly deformed. As shown in Fig. 2F (bottom), the width of the droplet on the right dramatically increases at 15 seconds. When the droplet (right) arrived at the center of MF-3, the two droplets tended to depress and merge to reduce the surface energy of the system, resulting in a decrease in width. Eventually, the two droplets merged into one larger droplet. Compared to passive coalescence, the droplets merged faster under an applied magnetic field (Fig. S8†) because the dewetting of the ferrofluid could lead to a consequently reduced ferrofluid film trapped between the droplets.

These results give evidence for droplet gating and sorting by transporter manipulation. As shown in Fig. 2G and Movie S5,† the undyed droplet was selectively actuated to travel across the two dyed droplets (i) because magnetic fields for positioning two dyed droplets in the array have equal magnetic flux density to the one for guiding the undyed droplet. When the magnetic flux density of one of the dyed droplets was increased, the undyed droplet did not pass through but merged with the droplet at the bottom (ii).

Generality of the ferrofluid transporter

We investigated the feasibility of the transporter for biochemical applications. We first tested the actuation capability for droplets with different pH values ranging from 1 to 14 by analyzing the average velocity of droplet transportation. As shown in Fig. 3A, the average velocities of droplets with

different pH values displayed no significant differences, demonstrating the successful actuation regardless of pH. Additionally, four commonly used chemicals in bioassays, Dulbecco's modified Eagle medium (DMEM), fetal bovine serum (FBS), lysogeny broth (LB), and PEG 20 000 (6 g in 10 mL, 65 mPa s) were adopted for demonstration. As shown in Fig. 3B, droplets were successfully transported. Moreover, various other plastic materials such as PE and PVC were used in cell culture and biochemical experiments. As shown in Fig. 3C, the droplet was successfully transported in different containers, indicating a universal droplet transport system. Rapid mixing of the droplet is important for biochemical reactions. Under passive mixing, the mixing of the droplet depends strongly on the Brownian diffusion of molecules. Fig. 3D shows that the uniform mixing of the merged droplet under passive mixing took over 150 s. However, back-and-forth transportation induced chaotic advection facilitates rapid mixing. The merged droplet was rapidly and uniformly mixed at 12 s under active mixing (Fig. 3D). Moreover, perfluorinated oil is widely used in droplet manipulation systems because of the low solubility of analytes in it. We incubated droplets containing rhodamine 6G in the system for 24 hours and confirmed that there is low risk of molecular diffusion (Fig. S9†).

Capillary force induced wrapping is possible for droplets with all length scales.[37] A 2 mL water droplet and a 4 mL water droplet were wrapped using a volume of 1 μL of ferrofluid transporter. When applying an external magnetic field in the middle, those two droplets were transported (Fig. 3E). The calculated average velocities before 22 s are 0.26 mm s^{-1} and 0.07 mm s^{-1} for 2 mL droplet and 4 mL droplet (Fig. 3E), respectively, which verifies successful wrapping and transportation. The transportation of a large volume droplet reflects a unique but counterintuitive feature of the transporter: a small-volume vehicle to transport large-volume cargos. In addition to a droplet, as glass sphere with a diameter of 1 μm could be wrapped by the transporter and transported in oil (Fig. 3G), implying the capability for solid cargo delivery in oil. Moreover, the transporter can actuate droplets against gravity (Fig. S10†). The results indicate that the ferrofluid transporter is a general and powerful toolbox for droplet manipulation.

Transporter manipulated on-chip droplet array and target delivery

The transporter can be used for on-chip droplet array fabrication. First, array arranged magnets were used for building the magnetic field array. Because of the magnetic responsiveness, the ferrofluid was pinned at each magnetic field center. When the droplet is injected to each ferrofluid location, the ferrofluid wraps and positions the droplet, forming the droplet array (Fig. S11†). Accordingly, an 8 × 9 droplet array was successfully fabricated, as shown in Fig. S11B.† Before demonstrating the capability of the transporter for target delivery in the droplet array, we investigated the biocompatibility of the system. Silicone oil bath provides a stable liquid environment protecting the droplet from evaporation, and silicone oil and fluorinated oil have been widely used in diagnostics and cell engineering.[38–40] Based on this, it is predicted that droplets on the transporter-manipulated array can serve as bio-incubators. To verify this, droplets with a volume of 1 μL containing GFP-*E. coli* were injected to the ferrofluid array to fabricate an 8 × 9 droplet array. After incubation for 24 hours, the fluorescence signal of each droplet was greatly enhanced (Fig. 4A), compared with the initial status in Fig. S12C.† To quantify the incubation, six droplets of the above sample were randomly picked for plate counting, and six groups with GFP-*E. coli* incubated in the tube were used as control samples. As shown in the graph in the inset in Fig. 4A, the count numbers of colonies in six randomly picked droplets and six non-droplet incubation samples display no significant differences. The results indicated the capability of the transporter manipulated droplet array for bio-incubation.

It is generally difficult to access each droplet in the array for the automated addition of drugs due to a lack of a flexible liquid-handling robot.[6] As previously mentioned, droplets can be transported through two positioned droplets and selectively merge with one of the droplets. We demonstrated that this capability can be further expanded to transport droplets in a complicated droplet array. A 5 × 6 droplet array was adopted for demonstration, and a micro-syringe was used to inject new droplets (target) onto the chip (Fig. 4B and Movie S6,† at 2.23 s). The transporter was guided to contact and wrap the target. As shown in Fig. 4B, the wrapped droplet was successfully delivered (at 21.12 s) and finally merged with the positioned droplet at the right bottom at 41.25 s. At the same time, a new injected droplet was wrapped and delivered in the droplet array to merge with other positioned droplets in the array. For high throughput screening, minimizing droplet sizes is of great importance. In the system, the droplet volume can be minimized to nanoliters. As shown in Fig. 4C, an array with each droplet having a volume of 20 nL (fluorescence droplets) was successfully established on the transporter-manipulated chip. Moreover, target delivery is still applicable in a miniaturized droplet array. As shown in Fig. 4C and Movie S7,† the droplet in the middle of the array was successfully transported away, and a new droplet (100 nL) was transported to that position. We showed the lossless transportation by testing the fluorescence intensity during the movement of the small droplet and concluded that no fluorescence trace was observed after the droplet was removed from the chip (Fig. S12†). In summary, with this wide ranging capability, this digital droplet chip is ready for bio-incubation and high throughput drug screening.

Application in on-chip droplet-based bioanalysis

Precise and lossless control of samples ensures the reliability of droplets as microreactors for sample processing and analysis in cell engineering and molecular diagnosis.[14,20,25] We illustrated the reliability of the transporter manipulation by adopting the polymerase chain reaction (PCR). As shown in Fig. 5A and Movie S8,† the transporter was programmed to perform sample wrapping, transportation, droplet merging, and mixing. In detail, droplets with target and reaction buffer were placed at magnetic field centers. Then, the two transporters (5 μL for each) were actuated to wrap sample droplets (2 μL each, with and without target) when corresponding magnetic fields were turned on. By switching to other magnetic fields, sample droplets were transported to merge with reaction droplets (8 μL for each). After mixing, mixtures were directly transferred into a thermal cycler for reaction. PAGE results for in-droplet experiments are in good agreement with those for control sets for positive and blank samples (Fig. 5B), demonstrating the feasibility of transporter manipulated sample processing for diagnostics. Among all read-out strategies, such as Raman spectroscopy and fluorescence, colorimetric detection is advantageous due to its direct read-out using the naked eye.[26,41] The dewetting phenomenon upon the application of an applied magnetic field facilitates the colour observation from the side-view (Fig. S13†), which is appropriate for a transporter system coupled with visualization technologies for on-site detection. We explored this potential of the transporter by detecting nitrite, as depicted in Fig. 5C. A droplet (5 μL) with nitrite was first transported to the camera acquisition center, and the Griess reagent (5 μL) was sequentially transported to merge with the droplet. The merged droplet was transported back-and-forth for mixing. After 30 min of reaction, photos of droplets with different concentrations of nitrite were recorded (Fig. 5D). Droplets containing higher concentrations of nitrite become most pronounced in colour after reaction. The measured absorbances of droplets with different concentrations show good linearity (Fig. 5E). With a computer-version-assisted signal readout system, it is expected that the transporter manipulation can be applied to rapid on-site biosensing.

Application in on-chip cell spheroid culture and drug screening

Human follicle dermal papilla cells (HFDPCs) are a group of specialized mesenchymal stem cells located at the bottom of the hair follicle.[42] Culturing HFDPCs in a 3D environment provides a more physiologically relevant model that closely mimics the native microenvironment of the hair follicle.[43] It is well known that excessive reactive oxygen species (ROS) will impair the cellular function of HFDPCs and trigger their apoptosis, which is highly associated with hair loss and other dermatological scalp conditions.[44,45] Rapid screening of ROS scavengers that could reduce ROS levels in 3D cultured HFDPCs can potentially provide therapeutic benefits against the oxidative stress-rich microenvironment in patients with alopecia. In this section, we used HFDPCs for proof of a 3D culture and drug screening demonstration. Since L-ascorbic acid (L-AA) and N-acetyl cysteine (NAC) can reduce the reactive oxygen (ROS) level, we investigated the effects of L-AA and NAC on the reduction of the ROS level in HFDPC spheroids using a hypoxia model.

First, we verified the feasibility for 3D cell culture. The ferrofluid accumulated at the bottom of the micro-sized droplet not only plays the role of positioning but also provides a smooth curvature to assist cell spheroid formation.[46–48] Later, 1 μL of encapsulated HFDPCs in a cell medium was injected onto the chip by a micro-syringe (1 μL). The chip was incubated at 37 °C in 5% CO_2, and the status of cells at different times was recorded. As shown in Fig. 6B, HFDPCs gradually aggregated inside the droplet and formed cell spheroids after 24 hours. We tested 24 droplets containing HFDPCs and all of them formed spheroids, illustrating good reproducibility (Fig. S14†). Moreover, HFDPCs in the cell spheroid structure exhibited high cell viability. We tested dead cells in cell spheroids incubated after day 1, day 2 and day 4, as shown in Fig. 6C. Only a few cells were dead inside the cell spheroid after 4 days of incubation, showing no significant difference compared with results after day 1 and day 2 (Fig. 6D). Note that during culturing on the transporter-manipulated chip, the culture medium was not refreshed. For comparison, HFDPCs were incubated in a 2D monolayer culture without medium refreshment, and a large number of dead cells were observed (Fig. 6E and S15†).

After verifying the feasibility for 3D cell culture, we present an 'all-in-one' droplet chip using a transporter for cell spheroid culture, drug delivery, and in situ screening, as shown in Fig. 6A. The chip contains a drug injection region with a micro-syringe inlet and a 5 × 6 droplet array for cell incubation. Overall, 30 droplets (in the 5 × 6 droplet array) encapsulated HFDPCs in the cell medium at the cell incubation region and were incubated for 24 hours. When HFDPCs formed cell spheroids, droplets with volumes of 10 μL containing 1 mM H_2O_2 and LAA with four concentrations of 10/100/150/200 μM or NAC with four concentrations of 4/20/30/40 mM were sequentially injected onto the chip using the micro-syringe (50 μL). Each drug droplet was transported by the ferrofluid transporter to merge with different positioned cell spheroid droplets, and the drug treated droplet array was incubated at 37 °C in 5% CO_2 for 2 hours. Three parallel experiments were successfully conducted on one chip, screening two different drugs, with each having four different concentrations. One group of fluorescence images for different drug treated cell spheroids is displayed in Fig. 6F, and the calculated cell viabilities are shown in Fig. 6G. The results indicate that cell spheroids treated with 10 and 100 μM of L-AA and 4 and 20 mM of NAC are mostly dead after being incubated for 2 hours, in contrast to the control group.

Meanwhile, high concentrations of L-AA (150 and 200 μM) and NAC (30 and 40 mM) result in fewer dead cells compared to other concentrations. This may be due to high concentrations of L-AA (150 and 200 μM) and NAC (30 and 40 mM) effectively reducing the ROS level in droplets (Fig. S16†).

Conclusions

In summary, we proposed a ferrofluid transporter as a multifunctional droplet manipulation system for integrating digital actuation to meet the needs of various biomedical and biochemical applications. The ferrofluid transporter wraps contacted droplets and manipulates them without the need for particle invasion. In the system, silicone oil sealing provides a stable environment. In addition, analytes have low solubility in perfluorinated oil (PFPE) used in droplet manipulation systems, thus it has no influence on most reactions. To stabilize droplets in traditional microfluidics, adding surfactant is a common approach. Meanwhile, in our system, droplets are stabilized by transporter positioning, and no surfactant was used. In addition, we demonstrated the digital actuation of transporter-carried droplets and showed that the transporter can manipulate droplets with a wide range of volumes (from the nL to mL scale), significantly extending the size limitation of actuated droplets, which cannot be achieved with current surface engineering methods. We verified the mechanism of the droplet actuation, for which the magnetic force can be programmed to actuate specific droplet motions, including the positioning of the droplet array, controlled droplet gating and sorting, as well as droplet merging and mixing. The transporter-based actuation offers great potential in biomedical applications, as it can transport droplets with a broad range of compositions and even solid particles. Given the high feasibility in biomedical applications, we demonstrated the application of transporters in *in vitro* bioanalysis involving nucleic acid and nitrite detection and proved the possibility of colorimetric-based detection. In addition, we developed a digital droplet chip and demonstrated its high feasibility for cell spheroid culture and high-throughput drug screening. From a future perspective, transporter-enabled digital droplet manipulation strategy can provide a toolbox for all droplet-based bioanalytical applications, particularly high-throughput analysis.

Author contributions

X. Y. supervised the project. X. Y. and X. W. designed the experiment. X. W. conducted droplet actuation experiments with assistance from H. B. S., X. L., C. C., A. L. and Z. T. H. B. S., A. L., and Z. T. contributed to the fabrication of ferrofluids. X. L. helped with mechanical analysis. C. C. contributed to PCR detection and chemical analysis. A. P. contributed to cell incubation. All authors participated in data analysis and manuscript drafting.

Conflicts of interest

There are no conflicts to declare.

Acknowledgements

Notes and references

1 H. Chen, P. Zhang, L. Zhang, H. Liu, Y. Jiang, D. Zhang, Z. Han and L. Jiang, *Nature*, 2016, **532**, 85–89.

2 X. Yao, Y. Hu, A. Grinthal, T. S. Wong, L. Mahadevan and J. Aizenberg, *Nat. Mater.*, 2013, **12**, 529–534.

3 J. El-Ali, P. K. Sorger and K. F. Jensen, *Nature*, 2006, **442**, 403–411.

4 D. S. Juang, T. D. Juang, D. M. Dudley, C. M. Newman, M. A. Accola, W. M. Rehrauer, T. C. Friedrich, D. H. O'Connor and D. J. Beebe, *Nat. Commun.*, 2021, **12**, 4317.

5 S. Sart, G. Ronteix, S. Jain, G. Amselem and C. N. Baroud, *Chem. Rev.*, 2022, **122**, 7061–7096.

6 S. P. Zhao, Y. Ma, Q. Lou, H. Zhu, B. Yang and Q. Fang, *Anal. Chem.*, 2017, **89**, 10153–10157.

7 A. J. DeMello, *Nature*, 2006, **442**, 394–402.

8 S. Battat, D. A. Weitz and G. M. Whitesides, *Lab Chip*, 2022, **22**, 530–536.

9 S. Feng, P. Zhu, H. Zheng, H. Zhan, C. Chen, J. Li, L. Wang, X. Yao, Y. Liu and Z. Wang, *Science*, 2021, **373**, 1344–1348.

10 T. S. Wong, S. H. Kang, S. K. Tang, E. J. Smythe, B. D. Hatton, A. Grinthal and J. Aizenberg, *Nature*, 2011, **477**, 443–447.

11 J. Jiang, J. Gao, H. Zhang, W. He, J. Zhang, D. Daniel and X. Yao, *Proc. Natl. Acad. Sci. U. S. A.*, 2019, **116**, 2482–2487.

12 D. Xia, L. M. Johnson and G. P. Lopez, *Adv. Mater.*, 2012, **24**, 1287–1302.

13 Q. Sun, D. Wang, Y. Li, J. Zhang, S. Ye, J. Cui, L. Chen, Z. Wang, H. J. Butt, D. Vollmer and X. Deng, *Nat. Mater.*, 2019, **18**, 936–941.

14 Y. Jin, W. Xu, H. Zhang, R. Li, J. Sun, S. Yang, M. Liu, H. Mao and Z. Wang, *Proc. Natl. Acad. Sci. U. S. A.*, 2022, **119**, e2105459119.

15 J. Li, N. S. Ha, T. Liu, R. M. van Dam and C. J. cj' Kim, *Nature*, 2019, **572**, 507–510.

16 W. Lei, G. Hou, M. Liu, Q. Rong, Y. Xu, Y. Tian and L. Jiang, *Sci. Adv.*, 2018, **4**, eaau8767.

17 Y. Xia, J. Li, L. X. Huang, B. Hua and S. S. Guo, *Anal. Chem.*, 2022, **94**, 6347–6354.

18 F. Wang, M. Liu, C. Liu, Q. Zhao, T. Wang, Z. Wang and X. Du, *Sci. Adv.*, 2022, **8**, eabp9369.

19 G. Kwon, D. Panchanathan, S. R. Mahmoudi, M. A. Gondal, G. H. McKinley and K. K. Varanasi, *Nat. Commun.*, 2017, **8**, 14968.

20 X. Wang, Z. Zhuang, X. Li and X. Yao, *Small Methods*, 2023, 2300253.

21 A. D. Ruvalcaba-Cardenas, P. Thurgood, S. Chen, K. Khoshmanesh and F. J. Tovar-Lopez, *ACS Appl. Mater. Interfaces*, 2019, **11**, 39283–39291.

22 H. Li, R. Chen, X. Zhu, Q. Liao, D. Ye, Y. Yang, W. Li, D. Li and Y. Yang, *Ind. Eng. Chem. Res.*, 2021, **60**, 3758–3769.

23 A. F. Demirors, S. Aykut, S. Ganzeboom, Y. A. Meier and E. Poloni, *Proc. Natl. Acad. Sci. U. S. A.*, 2021, **118**, e2111291118.

24 P. Dunne, T. Adachi, A. A. Dev, A. Sorrenti, L. Giacchetti, A. Bonnin, C. Bourdon, P. H. Mangin, J. M. D. Coey, B. Doudin and T. M. Hermans, *Nature*, 2020, **581**, 58–62.

25 A. Li, H. Li, Z. Li, Z. Zhao, K. Li, M. Li and Y. Song, *Sci. Adv.*, 2020, **6**, eaay5808.

26 H. Lin, W. Yu, K. A. Sabet, M. Bogumil, Y. Zhao, J. Hambalek, S. Lin, S. Chandrasekaran, O. Garner, D. Di Carlo and S. Emaminejad, *Nature*, 2022, **611**, 570–577.

27 C. H. Chiou, D. J. Shin, Y. Zhang and T. H. Wang, *Biosens. Bioelectron.*, 2013, **50**, 91–99.

28 M. A. Bijarchi, A. Favakeh, E. Sedighi and M. B. Shafii, *Sens. Actuators, A*, 2020, **301**, 111753.

29 Y. Zhang and T. H. Wang, *Adv. Mater.*, 2013, **25**, 2903–2908.

30 W. Yu, H. Lin, Y. Wang, X. He, N. Chen, K. Sun, D. Lo, B. Cheng, C. Yeung, J. Tan, D. D. Carlo and S. Emaminejad, *Sci. Robot.*, 2020, **5**, eaba4411.

31 Y. Zhou, S. Huang and X. Tian, *Adv. Funct. Mater.*, 2019, **30**, 1906507.

32 J. Zhang, X. Wang, Z. Wang, S. Pan, B. Yi, L. Ai, J. Gao, F. Mugele and X. Yao, *Nat. Commun.*, 2021, **12**, 7136.

33 W. Wang, J. V. I. Timonen, A. Carlson, D. M. Drotlef, C. T. Zhang, S. Kolle, A. Grinthal, T. S. Wong, B. Hatton, S. H. Kang, S. Kennedy, J. Chi, R. T. Blough, M. Sitti, L. Mahadevan and J. Aizenberg, *Nature*, 2018, **559**, 77–82.

34 E. J. G. Cartagena, I. Arenas, M. Bernardini and S. Leonardi, *Flow, Turbul. Combust.*, 2018, **100**, 945–960.

35 Y. Zeng, J. W. Khor, T. L. van Neel, W. C. Tu, J. Berthier, S. Thongpang, E. Berthier and A. B. Theberge, *Nat. Rev. Chem.*, 2023, **7**, 439–455.

36 K. Zimny, B. Mascaro, T. Brunet, O. Poncelet, C. Aristegui, J. Leng, O. Sandre and O. Mondain-Monval, *J. Mater. Chem. B*, 2014, **2**, 1285–1297.

37 B. Widom, *Phys. Today*, 2004, **57**, 66–67.

38 S. P. Zhang, J. Lata, C. Chen, J. Mai, F. Guo, Z. Tian, L. Ren, Z. Mao, P. H. Huang, P. Li, S. Yang and T. J. Huang, *Nat. Commun.*, 2018, **9**, 2928.

39 C. Liu, X. Liu, Q. Tang, W. Zhou, Y. Ma, Z. Gong, J. Chen, H. Zheng and S. W. Joo, *Anal. Chem.*, 2022, **94**, 8217–8225.

40 B. Zhao, C. W. MacMinn and R. Juanes, *Proc. Natl. Acad. Sci. U. S. A.*, 2016, **113**, 10251–10256.

41 T. AbdElFatah, M. Jalali, S. G. Yedire, I. I. Hosseini, C. Del Real Mata, H. Khan, S. V. Hamidi, O. Jeanne, R. Siavash Moakhar, M. McLean, D. Patel, Z. Wang, G. McKay, M. Yousefi, D. Nguyen, S. M. Vidal, C. Liang and S. Mahshid, *Nat. Nanotechnol.*, 2023, **18**, 922–932.

42 J. Hyun, J. Im, S. W. Kim, H. Y. Kim, I. Seo and S. H. Bhang, *Pharmaceutics*, 2021, **13**, 1155.

43 M. Bejaoui, A. K. Oliva, M. S. Ke, F. Ferdousi and H. Isoda, *Cells*, 2022, **11**, 2093.

44 J. H. Upton, R. F. Hannen, A. W. Bahta, N. Farjo, B. Farjo and M. P. Philpott, *J. Invest. Dermatol.*, 2015, **135**, 1244–1252.

45 S. Luanpitpong, U. Nimmannit, P. Chanvorachote, S. S. Leonard, V. Pongrakhananon, L. Wang and Y. Rojanasakul, *Apoptosis*, 2011, **16**, 769–782.

46 H. Cui, T. Tronser, X. Wang, J. Wesslowski, G. Davidson, A. A. Popova and P. A. Levkin, *Droplet*, 2022, **2**, e39.

47 T. E. de Groot, K. S. Veserat, E. Berthier, D. J. Beebe and A. B. Theberge, *Lab Chip*, 2016, **16**, 334–344.

48 H. Li, P. Liu, G. Kaur, X. Yao and M. Yang, *Adv. Healthcare Mater.*, 2017, **6**, 1700185.